International Journal of Computer Information Systems and Industrial Management Applications
ISSN 2150-7988 Volume 18(9s) 2026 pp. 1298-1312
https://doi.org/10.70917/ijcisim-2026-3554
Article

Ionospheric Effects of the X9.3 Solar Flare of 6 September 2017 on Earth and Mars: A Comparative Study of Density, Temperature, and Plasma Upflow

Ashish Kumar Meena[1*], Purushotham Endla[2]

[1,2]School of Sciences and Humanities (Physics), SR University, Warangal, Telangana - 506371, India
Corresponding Author; [1*]Email: ashishmeena944@gmail.com
ORCID: [1]https://orcid.org/0000-0002-1674-0252 , [2]https://orcid.org/0000-0001-8412-5932

Abstract: Solar flares are known to strongly perturb the ionospheres of terrestrial planets through sudden enhancements in X-ray and extreme-ultraviolet (EUV) irradiance, yet relatively few studies have directly compared how this perturbation unfolds on different Earth-like bodies. Here we use two self-consistent, one-dimensional planetary ionosphere models to simulate how the Earth and Mars ionospheres responded to the solar flares of 6 September 2017. Both planets show a clear rise in electron density in the lower ionosphere, although the magnitude of this enhancement differs considerably between them. Ion-temperature responses are broadly similar at the two planets, with the background neutral atmosphere responsible for the differences that do appear. For the X9.3 flare, the electron temperature at Earth rises by as much as 250 K, whereas at Mars it instead falls by roughly 40 K. Both planets also develop an enhanced upward plasma velocity during the flare, and the resulting upward flux grows by 2.16 × 1012 m^{-2} s^{-1} at 800 km at Earth and by 8.45 × 109 m^{-2} s^{-1} at 400 km at Mars. To our knowledge, this is the first self-consistent simulation to reproduce a flare-driven enhancement of upward plasma flow at Mars.

Graphical Abstract

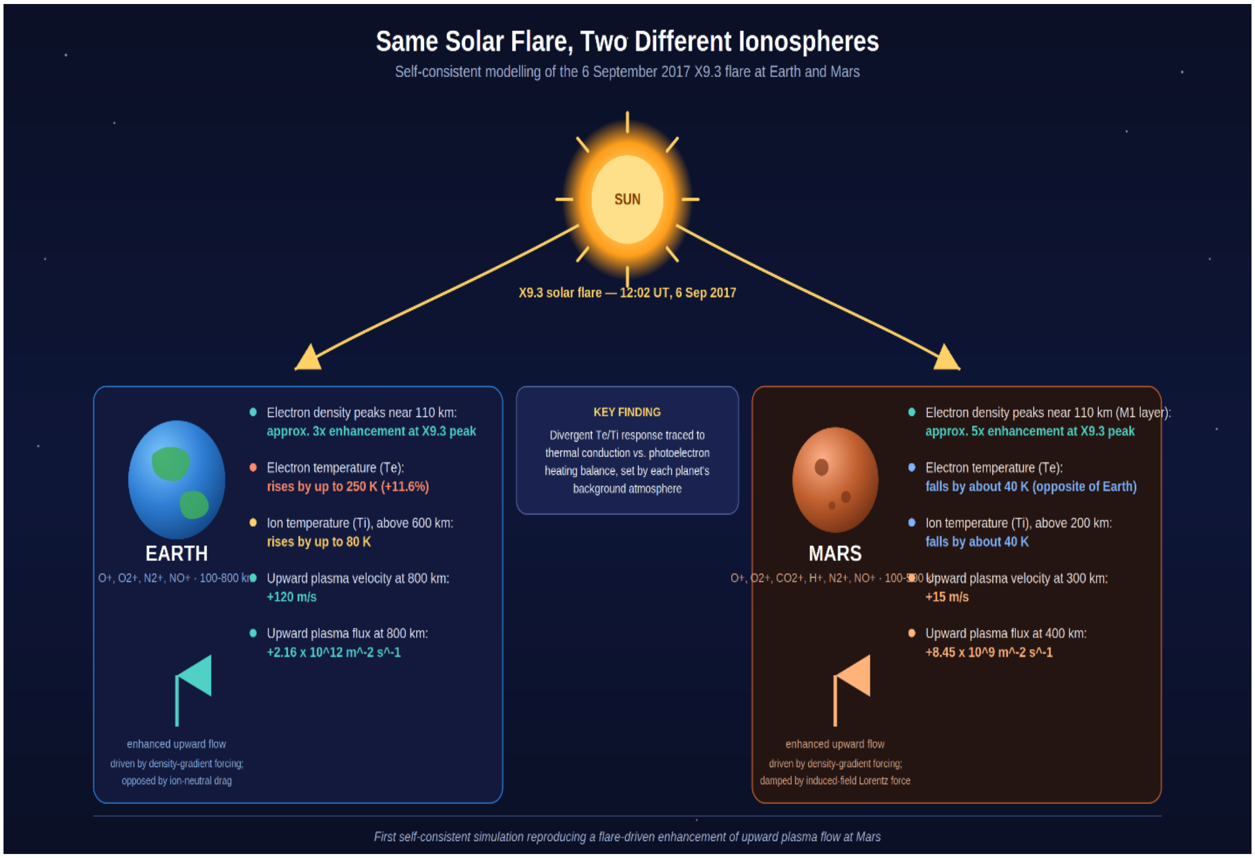

Highlights

A Self-Consistent Comparison of Ionospheric Responses at Earth and Mars to the 6 September 2017 Solar Flares

- First self-consistent Earth-Mars comparison of flare-driven ionosphere response.
- Electron density in the lower ionosphere rises during the flare at both planets.
- Electron temperature rises 250 K at Earth but falls about 40 K at Mars.
- Ion temperature rises at Earth above 600 km but falls at Mars above 200 km.

First self-consistent simulation of flare-driven upward plasma flow at Mars.

Keywords: Ion Temperature, Earth, Mars, Solar Flare (SF), Ionosphere

1. Introduction

The ionosphere of a terrestrial planet arises from photoionization of its neutral atmosphere by solar X-ray and extreme-ultraviolet (EUV) radiation. Spacecraft missions have characterized the ionospheres of Earth and Mars in detail (Todorova et al., 2008; Mendillo et al., 2011; Futaana et al., 2017); Figure 2, presented in Section 3, compares the two and illustrates how differences in background atmosphere, magnetic environment, and distance from the Sun shape their respective ionospheric structures (Schunk & Nagy, 1980). The irradiance that drives the ionosphere is far from constant it varies over the 11-year solar cycle, over the 27-day solar rotation period, on a daily basis, and impulsively during solar flares that last only tens of minutes (Sátori et al., 2005; Mendillo et al., 2006; Ren et al., 2018). A solar flare is a sudden burst of radiation from an active region of the corona, dominated by a rapid brightening in the EUV and soft X-ray bands. This extra irradiance drives additional ionization, dissociation, and heating throughout the ionosphere (Lollo et al., 2012), disturbing plasma density, temperature, and dynamics. Foundational studies of the terrestrial ionosphere's flare response (Mitra, 1974; Davies, 1990) have since been extended by more detailed comparative work on Earth and Mars (Yamauchi et al., 2018; Qian et al., 2019), although the Martian response has received comparatively little attention beyond early studies such as Kar et al. (1986). Related case studies of ionospheric behaviour during other recent solar and geomagnetic disturbances, including the ionospheric response over low-latitude Asia to the September 2017 storms, moderate flare and ion-composition changes in January 2023, the correlation between solar-activity indices and geomagnetic disturbances through 2023, the response to moderate flares of 5-7 August 2023, and total electron content changes during strong and weak flares near the 2011 solar peak, have also been reported (Meena & Gour, 2024; Meena et al., 2024a; Gour et al., 2024; Meena et al., 2024b; Meena et al., 2024c). A consistent picture emerges from this body of work: electron density rises most strongly in the lower ionosphere of both planets near 115 km in Earth's E layer and in the Martian M1 layer during a flare. Ground- and satellite-based measurements further show that both electron and ion temperatures at Earth increase in response to the extra high-energy radiation (Sharma et al., 2004), whereas observations of the 10 September 2017 flare at Mars instead found a temperature decrease below 225 km, attributed to an expansion of the neutral atmosphere (Thiemann et al., 2018). Flares have also been shown to heat and inflate the upper neutral atmospheres of both planets, feeding back onto their ionospheres (Qian et al., 2019).

September 2017 was an especially active period, with several major flares emerging from active region 2673 (Lee et al., 2018). Figure 1 shows the GOES soft X-ray irradiance (0.1–0.8 nm) recorded on 6 September 2017, a day on which two major flares occurred: an X2.2 event peaking at 09:10 UT and an X9.3 event the strongest flare of solar cycle 24 peaking at 12:02 UT. This study focuses on the ionospheric response to the X9.3 flare. Incoherent-scatter radar measurements from the Millstone Hill Observatory captured a marked increase in the upward plasma drift, and in the corresponding escape rate, at Earth during this event (Mendillo et al., 2018). Comparing the responses to the flares of 6 and 10 September, Qian et al. (2019) and Owolabi et al. (2020) found that Earth's thermosphere–ionosphere system reacted differently to disk-center versus limb flares, a contrast they attributed to differences in the associated EUV enhancement.

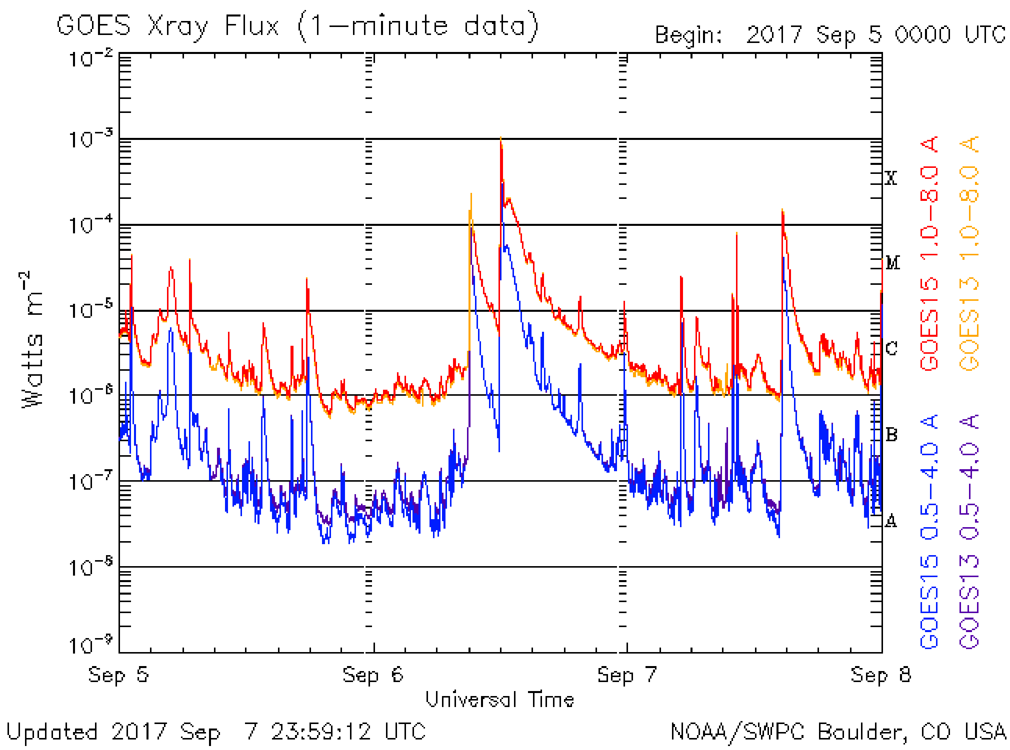

Figure 1. GOES-15 soft X-ray irradiance (0.1–0.8 nm) on 6 September 2017, showing the X2.2 flare (09:10 UT) and the X9.3 flare (12:02 UT).

Most existing work on flare-driven ionospheric change has examined a single planet at a time; the studies of Mendillo et al. (2006, 2018) are a notable exception in directly comparing Earth and Mars. A systematic comparison spanning all three terrestrial planets one capable of separating the physics common to all of them from the physics specific to each was recently undertaken for Earth, Venus, and Mars by Yan et al. (2022), who also reported a self-consistent simulation of flare-driven upward plasma flow at Mars; the present study instead focuses specifically on the Earth-Mars comparison. We address part of this gap by assuming that the flares of 6 September 2017 illuminated Mars as well as Earth, and by simulating how the ionospheres of the two planets respond to the same rapid brightening event. We do not attempt to account for any difference in flare phase or arrival time that Earth and Mars would actually observe owing to their different orbital positions. Using newly developed, self-consistent ionospheric models for Earth and Mars, we examine how plasma density, temperature, and vertical velocity respond to the flare, and we identify the physical mechanisms responsible for the differences we find between the two planets.

2. Models of the Ionosphere for Earth and Mars

We constructed one-dimensional, self-consistent ionospheric models for Mars by extending the Earth model of Lei et al. (2004a, 2004b). The Earth model tracks four ion species O^+, $O2^+$, $N2^+$, and NO^+ between 100 and 800 km altitude. Our new Martian counterpart covers 100–500 km altitude and solves the coupled continuity and momentum equations for six ion species: O^+, $O2^+$, $CO2^+$, H^+, $N2^+$, and NO^+. Electron and ion temperatures are obtained from the corresponding energy equations, and the influence of the horizontal magnetic field is included, following the formulation of Shinagawa et al. (1987, 1991).

The equation describing the continuity of ions is

$$Q_i - \beta_i o_i = \frac{\partial o_i}{\partial U} + \frac{\partial (o_i X_i)}{\partial z} \quad \textbf{(1)}$$

The equation expressing the horizontal momentum for ions is provided as:

$$\left(\frac{\partial W_i}{\partial U} + X_i \frac{\partial W_i}{\partial a}\right) = \frac{r_i C}{n_i}(X_i - X_e) - \frac{n_e}{m_i}\text{Ven}\,(W_e - W_i) + V_{in}(W_i - W_e) \quad (\mathbf{2})$$

The equation describing the vertical momentum of ions is

$$\left(\frac{\partial X_i}{\partial u} + X_i \frac{\partial X_i}{\partial a}\right) = \frac{R_i B}{n_i}(W_e - W_i) - \frac{L}{n_i o_i}\frac{\partial (o_i \mathrm{V}_i)}{\partial \mathrm{a}} - \frac{L}{n_i o_e}\frac{\partial (o_e \mathrm{V}_e)}{\partial \mathrm{a}} - g - V_{in}(X_i - X_n) - \frac{n_e}{n_i}\mathrm{V}X_{en}\,(\mathrm{X}_e - X_i)$$

(3)

The mathematical expressions describing the energy equations for the electron and the prevalent ion are as follows:

$$\frac{3}{2}o_s \mathrm{l}\left(\frac{\partial U_s}{\partial u} + X_s \frac{\partial U_s}{\partial a}\right) = -o_s l U_s \frac{\partial X_s}{\partial a} + \frac{\partial}{\partial a}\left(k_s \frac{\partial U_s}{\partial a}\right) + R_s + M_s \quad (\mathbf{4})$$

The magnetic field's diffusion equation, derived from Maxwell's equations, can be expressed as

$$\frac{\partial C}{\partial u} + \frac{\partial}{\partial a}\left[-CX_e + \frac{n_e(V_{en} + V_{ei}}{o_e f^2 \mu_o}\ \frac{\partial c}{\partial a}\right] \quad (\mathbf{5})$$

The electron velocities in both horizontal and vertical directions are determined through the application of Maxwell's equations and the averaging of ion velocities. These velocities are then expressed in written form.

$$W_e = \frac{1}{o_e}\left(\sum_i o_i V_i - \frac{1}{f\mu_o}\frac{\partial c}{\partial a}\right) \quad (\mathbf{6})$$

$$X_e = \frac{1}{o_e}\sum_i o_i X_I \quad (\mathbf{7})$$

Here the subscript i denotes the primary ion species (O^+, $O2^+$, $CO2^+$, H^+, $N2^+$, and NO^+), the subscript e refers to electrons, and the subscript s covers both electrons and the major ions. The quantities g, l, and μ_0 are, respectively, the gravitational acceleration, the Boltzmann constant, and the permeability of free space; u and a denote time and vertical altitude. r_i is the ionic charge; o_i and o_e are the ion and electron densities; n_i and n_e are the ion and electron masses; Q_i and β_i are the ion production and loss rates. W_i and W_e are the horizontal ion and electron velocities, while X_i and X_e are the corresponding vertical velocities. Horizontal and vertical neutral winds, W_n and X_n, are set to zero throughout this study. V_{en}, V_{in}, and V_{ei} denote the electron–neutral, ion–neutral, and electron–ion collision frequencies, respectively; U_s is temperature, l_s is thermal conductivity, and R_s and M_s represent heating and cooling rates. C denotes the magnitude of the magnetic field.

For Earth, the solar spectrum used to drive the flare simulations combines GOES X-ray irradiance over 0.1–0.8 nm with the Flare Irradiance Spectral Model, Version 2 (FISM2; Chamberlin et al., 2020), over 0.8–175 nm. In the non-flare runs the background spectrum matches the flare simulation everywhere except across the flare interval

(08:50–16:00 UT), where irradiance is instead obtained by linear interpolation between the 08:50 and 16:00 UT values. This Earth-based spectrum is then scaled to the Mars orbital distance and, following an approach similar to Solomon (2017), divided into 120 wavelength bands for use in both models.

Absorption and ionization cross sections for O, O2, N2, and CO2 are taken from Conway (1988), Fennelly & Torr (1992), and Masuoka (1994). The Earth model obtains the ionization rate and associated photoelectron heating rate from the Global Airglow (GLOW) model (Solomon, 2017), assuming local energy degradation of photoelectrons; the Martian model applies the same GLOW framework after adjusting the background atmosphere and cross sections appropriately for Mars. The principal chemical reaction scheme in the Earth model follows Lei et al. (2004a), while the Martian scheme closely follows Martinis et al. (2003).

Although the neutral heating rate itself increases during a flare, we hold the neutral background of both planets fixed over the short interval considered here, following Smithtro et al. (2006); this keeps the focus on the ionospheric response to the flare rather than on the full coupled thermosphere–ionosphere system, and the implications of this simplification are revisited in the discussion. Neutral densities and temperatures come from the NRLMSIS-00 model (Picone et al., 2002) at Earth and from Fox & Sung (2001) and Fox et al. (2021) at Mars. Neutral winds at Earth are taken from the HWM07 model (Drob et al., 2008) and are neglected at Mars. Earth's internal magnetic field follows the International Geomagnetic Reference Field (IGRF) model (Barton, 1997); at Mars, the initial field profile instead represents the solar-wind-induced field, shown as the blue dashed curves in Figures 2(f) and 2(i).

The Earth simulations adopt an F10.7 proxy of 135 solar flux units, appropriate for 6 September 2017, in both the NRLMSIS-00 and HWM07 models. A spatial resolution of 2 km and a time step of roughly half a minute are used for both planets. At the lower boundary (100 km), the ions are assumed to be in photochemical equilibrium, at the local neutral temperature, with zero velocity; the magnetic field is set to zero at the Martian lower boundary. At the upper boundary (800 km at Earth, 500 km at Mars), fixed fluxes close the continuity, momentum, and energy equations (Shinagawa et al., 1987, 1991), and $\partial C/\partial a = 0$ closes the magnetic field equation. All results shown here correspond to a solar zenith angle of 60°, representative of average dayside conditions (Fox & Bakalian, 2001).

The altitude profiles of plasma density, temperature, and magnetic field produced by these two models for both planets together with the background ionospheric structure they establish — are presented and discussed in Figure 2 at the beginning of Section 3, alongside the flare-driven changes analysed in the remainder of this study.

3. Results

Figure 2 shows the modelled altitude profiles of plasma density (left column), temperature (middle column), and magnetic field (right column) at Earth and Mars, for the solar zenith angle of 60° adopted throughout this study. The two ionospheres share several qualitative features: each has a photochemistry-controlled layer at lower altitudes, where EUV photons (10–100 nm) ionize neutral molecules to form molecular ions, and transport effects only become important above roughly 200 km at both planets.

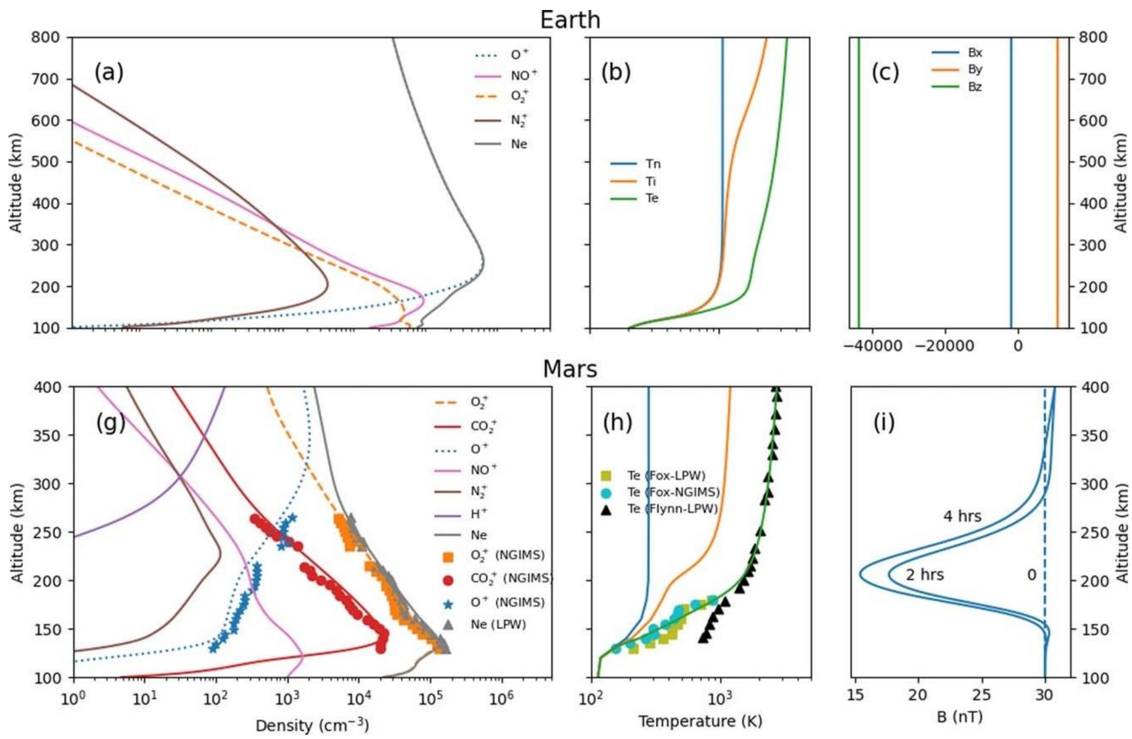

Figure 2. Simulated altitude profiles of ion and electron densities (left column), neutral (Tn), ion (Ti) and electron (Te) temperature (middle column), and magnetic field (right column) at a solar zenith angle of 60°, for Earth and Mars. Panel (c) shows Earth's internal magnetic field; panel (i) shows the induced field at Mars after 0, 2, and 4 hours. Panel (g) compares modelled $O2^+$, $CO2^+$, O^+, and electron densities with MAVEN NGIMS and LPW observations (orange squares, red circles, blue stars, and grey triangles). Panel (h) compares modelled and LPW/NGIMS-observed electron temperatures (olive squares, cyan circles, dark triangles).

Subpeaks in electron density, produced by soft X-ray radiation and photoelectron-impact ionization, appear near 110 km at both Earth (Figure 2a) and Mars (Figure 2g), and O^+ is the dominant ion in the high-altitude ionosphere of both planets. The two profiles nonetheless differ substantially, reflecting the very different background atmospheres and heliocentric distances of the two bodies. As the middle column of Figure 2 shows, electron temperature (Te) exceeds both ion (Ti) and neutral (Tn) temperature at higher altitudes on both planets, while below 130 km frequent ion–neutral and electron–neutral collisions keep all three temperatures nearly equal. Strong thermal conduction limits the variation of neutral temperature above 200 km, where Earth's neutral temperature (≈ 1000 K) is far higher than that of Mars (≈ 300 K). In the topside ionosphere the ordering reverses for the plasma temperatures: electron temperature at Mars exceeds that at Earth, while ion temperature at Earth exceeds that at Mars.

Our models reproduce the altitude and magnitude of the previously documented electron-density peak (the Martian M1 layer) and subpeak (the Martian M2 layer) (e.g., Fox & Sung, 2001; Fox et al., 2021). Figure 2 also compares the modelled Martian plasma densities and temperatures against MAVEN observations, showing broad agreement between model and data. Figure 2(i) traces the evolving induced/crustal magnetic field at Mars; owing to vertical convection, a minimum develops rapidly near 210 km, consistent with the behaviour reported in Figure 6 of Shinagawa & Cravens (1989). Earth's internal field, which does not evolve on these timescales, is shown for reference in Figure 2(c).

The sensitivity of ionospheric electron density to solar flares is well documented (e.g., Kar et al., 1986; Huba et al., 2005; Smithtro et al., 2006; Mendillo et al., 2006; Lei et al., 2007; Fallows et al., 2015): the surge in solar radiation during a flare drives a substantial rise in electron density. Figure 3 shows the ratio of electron density in the flare and no-flare simulations for Earth and Mars during the 6 September 2017 event. The X9.3 flare produces a larger and more persistent enhancement than the X2.2 flare at both planets. At the X9.3 peak (12:02 UT; Figures 3a and 3e), the strongest enhancement occurs at relatively low altitude, with peak ratios of about 3 at Earth and about 5 at Mars, consistent with photochemistry dominating the response at these altitudes (Rishbeth & Garriott, 1969). Several ion chemistry pathways together shape these peak values.

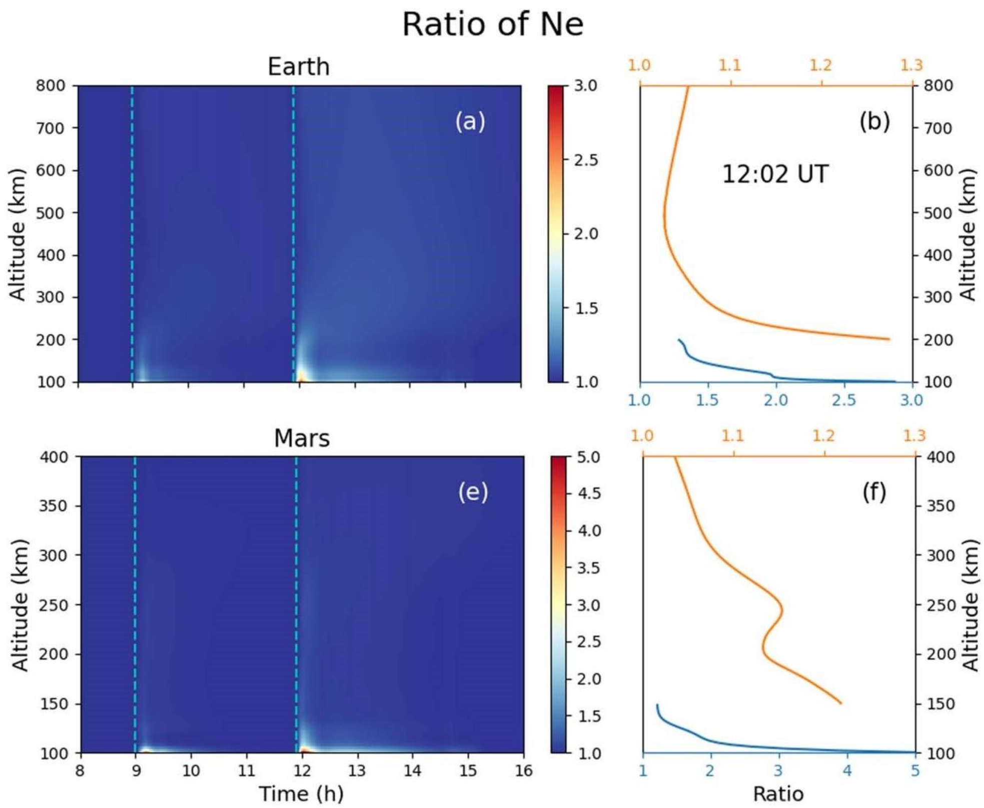

Figure 3. Relative change (ratio) in electron density between the flare and no-flare simulations at Earth (a) and Mars (e); vertical lines mark the onset of the two flares. Panels (b) and (f) show the altitude dependence of this ratio at the X9.3 peak (12:02 UT). In the right-hand panels, ratios above 1.25 are read against the bottom axis (blue) and ratios below 1.25 against the top axis (orange).

The flare enhances photoionization of N2+ at Earth and of CO2+ at Mars in the low-altitude ionosphere. At Earth, N2+ is subsequently converted to O2+ via N2+ + O2 → O2+ + N2 in the E region; at Mars, the analogous pathway converts CO2+ to O2+ via CO2+ + O → O2+ + CO. Because these molecular ions ultimately recombine with electrons at different rates, the two planets can show quite different peak enhancements in low-altitude electron density.

At higher altitude 500 km at Earth and 300 km at Mars the electron-density increase is smaller, about 2.8% and 8.3% respectively. In both cases the low-altitude response tracks the flare almost immediately, while the high-altitude response is delayed. This delay reflects the combined roles of photoionization and transport at high altitude (Smithtro & Solomon, 2008), where flare-enhanced plasma produced lower down is carried upward, and it may also partly reflect the slower rise of the EUV component of the flare relative to its soft X-ray and Lyman-α components.

Flares also disturb the energy balance of the ionospheric plasma. Figure 4 shows the absolute change, relative to the no-flare case, in electron temperature (left) and in the dominant ion temperature (right) at Earth and Mars during the 6 September 2017 event. The electron-temperature response at Mars differs markedly from that at Earth. At high altitude, ion temperature increases at Earth but decreases at Mars. At both planets the X2.2 flare produces a temperature response with the same shape as the X9.3 response but of smaller amplitude, and in both cases the response is concentrated at higher altitude: lower down, frequent ion–neutral collisions keep electron and ion temperature close to the unperturbed background.

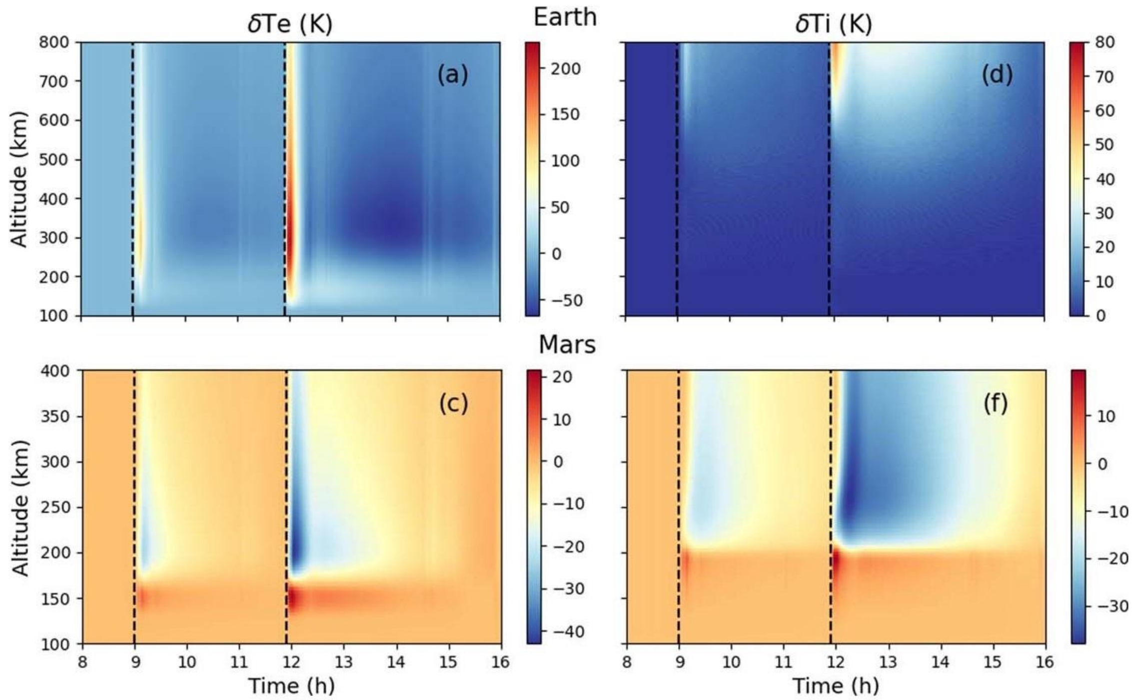

Figure 4. Absolute change in electron temperature (left) and dominant-ion temperature (right) induced by the flares at Earth and Mars. Vertical lines mark the onset of the two flares.

During a flare, the jump in solar irradiance increases the photoelectron population and, with it, the thermal electron heating rate (Schunk & Nagy, 1978); the accompanying rise in plasma density also alters the efficiency of thermal conduction and of electron–ion Coulomb collisions. At Earth, Figure 4(a) shows electron temperature rising by 250 K (11.6% above baseline) at the X9.3 peak; several hours later, the temperature near 300 km falls by about 50 K relative to baseline. A similar pattern was reported for the terrestrial X17 flare of 28 October 2003 by Smithtro & Solomon (2008), who attributed the peak increase to photoelectron heating and the subsequent decrease to enhanced electron–ion collisional cooling. The differences between the electron-temperature responses of Earth and Mars are examined further below.

Figures 4(d)–(f) show the ion-temperature responses at Earth and Mars. At Earth, ion temperature increases above 600 km (Figure 4d) by up to 80 K. At Mars (Figure 4f), ion temperature instead decreases by roughly 40 K above 200 km, with a smaller increase of about 15 K near 150 km. These density and temperature changes in turn affect the vertical dynamics of the plasma. Earlier work suggested that flares drive an enhanced upward plasma drift at Earth through the combined effect of increased electron density and temperature (e.g., Mendillo & Evans, 1974), and Mendillo et al. (2018) later predicted an analogous enhancement at Mars using an analytical one-dimensional model; however, no fully self-consistent model — solving the continuity, momentum, energy, and magnetic-field equations together had previously been used to simulate flare-driven upward plasma drift at either planet.

Figure 5 shows the absolute change in vertical plasma velocity between the flare and no-flare simulations at both planets. As with electron density and temperature, the X2.2 flare produces a much weaker velocity response than the X9.3 flare, likely reflecting the nonlinear dependence of the vertical dynamics on density and temperature. At the X9.3 peak (12:02 UT), the upward flow reaches about 120 m s^{-1} at 800 km at Earth and about 15 m s^{-1} at 300 km at Mars. The corresponding upward flux ($n_e W_e$) increases by 2.16 × 1012 $m^{-2} s^{-1}$ at 800 km at Earth consistent with the Millstone Hill radar observations shown in Figure 4 of Mendillo et al. (2018) and by 8.45 × 109 $m^{-2} s^{-1}$ at 400 km at Mars. Solar flares therefore drive an enhanced plasma upflow at both planets.

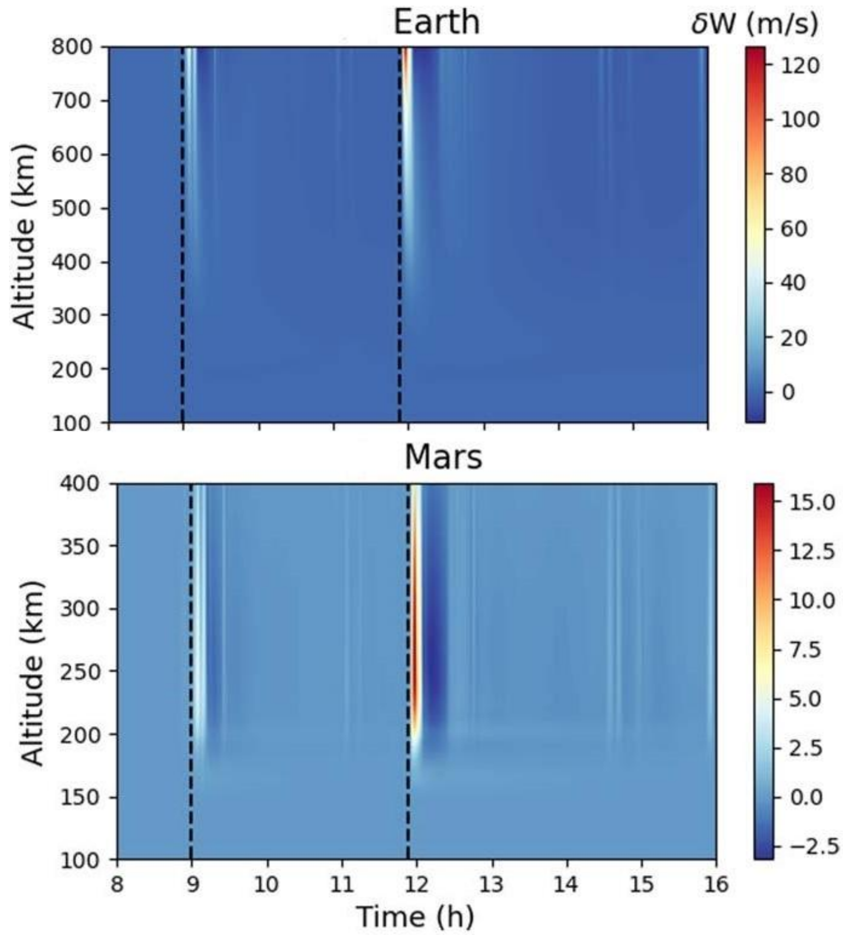

Figure 5. Change in vertical plasma velocity between the flare and no-flare simulations at Earth and Mars. Vertical lines mark the onset of the two flares.

4. Discussion

The results above describe how the ionospheres of Earth and Mars each respond to an identical pair of solar flares. Because photochemistry dominates at low altitude, the flare-driven rise in electron density is concentrated there at both planets. Alongside this density response, we also find substantial changes in plasma temperature and vertical velocity. Notably, when changes in the background neutral atmosphere are excluded from consideration, our simulations show that the flare actually reduces electron temperature at Mars the opposite of the Earth response. This work also provides, to our knowledge, the first self-consistent simulation of flare-driven enhancement of upward plasma flow at Mars. The remaining open question is what physical mechanism is responsible for the differing energetic and dynamical responses of the two planets to the same flare.

Ionospheric plasma temperature reflects a balance between several heating and cooling processes (Schunk & Nagy, 1978; Matta et al., 2014). During a flare, the increase in solar irradiance raises the photoelectron population and, with it, the thermal electron heating rate; at low altitude, exothermic ion–neutral chemical reactions are an important additional heat source for the ions, while at higher altitude thermal conduction and Coulomb collisions between electrons and ions become the dominant energy-transfer channels, both closely tied to electron density (Schunk & Nagy, 2009). Heating from photoelectrons and chemical reactions scales roughly linearly with the photoionization rate, or equivalently with electron density, whereas Coulomb-collision energy transfer scales closer to the square of electron density (Lei et al., 2007). The coefficients governing these terms, together with the efficiency of thermal conduction, depend on the local background density and temperature and therefore differ between the two planets, which is ultimately why their plasma-temperature responses in Figure 4 diverge. A similar competition between photoelectron heating and thermal conduction underlies the well-known morning electron-temperature overshoot documented at both Earth (Lei et al., 2007) and Mars (Pilinski et al., 2021). In our simulations, thermal-conduction cooling dominates above 200 km at Mars, producing the electron-temperature decrease seen in Figures 4(b)–(c), whereas the modest increase near 150 km is instead governed by photoelectron heating. The ion-temperature decline seen above 200 km at Mars in Figure 4(f) is likewise driven mainly by thermal conduction.

The equation describing the continuity of ions is

$$Q_i - \beta_i o_i = \frac{\partial o_i}{\partial U} + \frac{\partial (o_i X_i)}{\partial z} \quad \textbf{(1)}$$

The equation expressing the horizontal momentum for ions is provided as:

$$\left(\frac{\partial W_i}{\partial U} + X_i \frac{\partial W_i}{\partial a}\right) = \frac{r_i C}{n_i}(X_i - X_e) - \frac{n_e}{m_i} \mathrm{Ven}\ (W_e - W_i) + V_{in}(W_i - W_e) \quad (\mathbf{2})$$

The equation describing the vertical momentum of ions is

$$\left(\frac{\partial X_i}{\partial u} + X_i \frac{\partial X_i}{\partial a}\right) = \frac{R_i B}{n_i}(W_e - W_i) - \frac{L}{n_i o_i}\frac{\partial (o_i \mathrm{V}_i)}{\partial \mathrm{a}} - \frac{L}{n_i o_e}\frac{\partial (o_e \mathrm{V}_e)}{\partial \mathrm{a}} - g - V_{in}(X_i - X_n) - \frac{n_e}{n_i}\mathrm{V}X_{en}\ (\mathrm{X}_e - X_i) \quad \textbf{(3)}$$

The mathematical expressions describing the energy equations for the electron and the prevalent ion are as follows:

$$\frac{3}{2} o_s \mathrm{l}\left(\frac{\partial U_s}{\partial u} + X_s \frac{\partial U_s}{\partial a}\right) = -o_s l U_s \frac{\partial X_s}{\partial a} + \frac{\partial}{\partial a}\left(k_s \frac{\partial U_s}{\partial a}\right) + R_s + M_s \quad (\mathbf{4})$$

The magnetic field's diffusion equation, derived from Maxwell's equations, can be expressed as

$$\frac{\partial C}{\partial u} + \frac{\partial}{\partial a}\left[-C X_e + \frac{n_e(V_{en} + V_{ei}}{o_e f^2 \mu_o} \ \frac{\partial c}{\partial a}\right] \quad (\mathbf{5})$$

The electron velocities in both horizontal and vertical directions are determined through the application of Maxwell's equations and the averaging of ion velocities. These velocities are then expressed in written form.

$$W_e = \frac{1}{o_e}\left(\sum_i o_i V_i - \frac{1}{f \mu_o}\frac{\partial c}{\partial a}\right) \quad (\mathbf{6})$$

$$X_e = \frac{1}{o_e}\sum_i o_i X_I \quad (\mathbf{7})$$

Here the subscript i denotes the primary ion species (O^+, $O2^+$, $CO2^+$, H^+, $N2^+$, and NO^+), the subscript e refers to electrons, and the subscript s covers both electrons and the major ions. The quantities g, l, and μ_0 are, respectively, the gravitational acceleration, the Boltzmann constant, and the permeability of free space; u and a denote time and vertical altitude. r_i is the ionic charge; o_i and o_e are the ion and electron densities; n_i and n_e are the ion and electron masses; Q_i and β_i are the ion production and loss rates. W_i and W_e are the horizontal ion and electron velocities, while X_i and X_e are the corresponding vertical velocities. Horizontal and vertical neutral winds, W_n and X_n, are set to zero throughout this study. V_{en}, V_{in}, and V_{ei} denote the electron–neutral, ion–neutral, and electron–ion collision frequencies, respectively; U_s is temperature, l_s is thermal conductivity, and R_s and M_s represent heating and cooling rates. C denotes the magnitude of the magnetic field.

Figure 6(a) shows the time evolution, at 600 km altitude, of the density-gradient, temperature-gradient, and ion-neutral-drag (collisional) terms in Equation (10), comparing the flare and no-flare simulations at Earth. At Mars, vertical motion cannot be treated as steady-state (Equation 8), so the Lorentz-force and inertial ($\partial W_i/\partial u$) terms must also be retained; Figures 6(b) and 6(c) show the corresponding forcing terms at 300 km. Across all cases, the enhanced upflow seen in Figure 5 is primarily driven by the change in the plasma density gradient (orange curves in Figure 6). At Earth, ion-neutral drag opposes this upflow, reflecting more frequent collisions in the denser neutral atmosphere; at Mars, the Lorentz force instead provides the dominant restoring force, slightly damping the flare-driven upflow. Because flares enhance plasma density more strongly at lower than at higher altitude (right-hand column of Figure 3), the density-gradient forcing is the main driver of the flare-time upflow (Figure 5) at both planets, while ion drag and the Lorentz force act to partially oppose it.

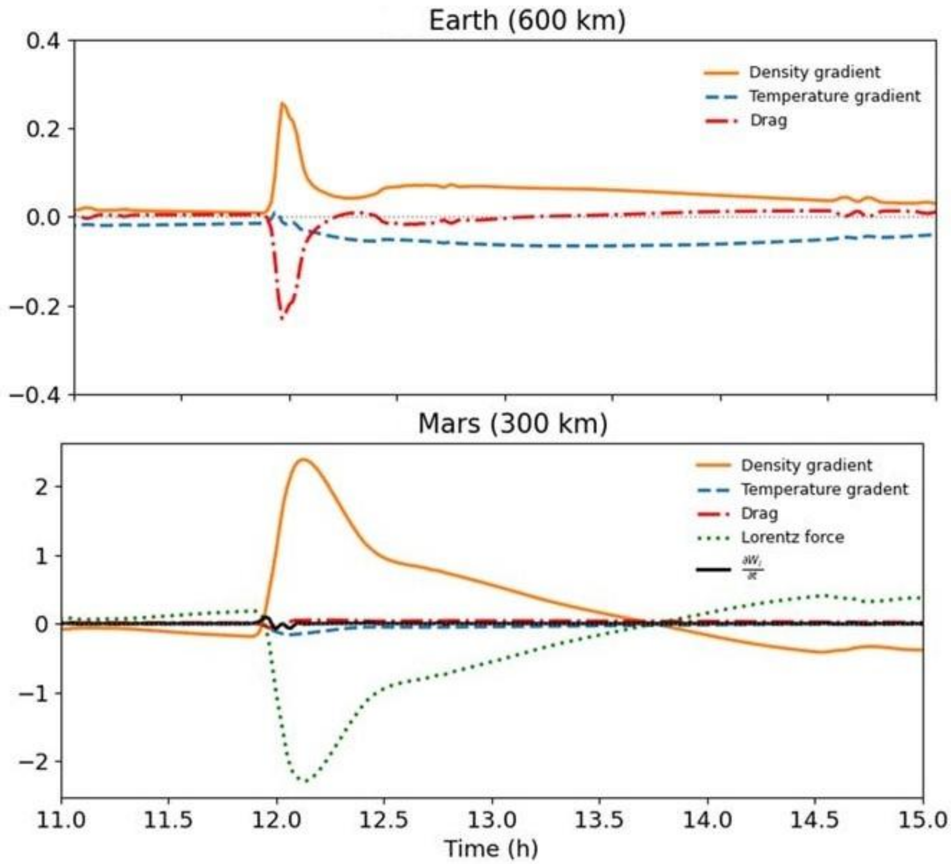

Figure 6. Term-by-term analysis of the differential force per unit mass on O^+ between the flare and no-flare simulations for the X9.3 event. Orange, blue, red, and green curves show the plasma-density-gradient, plasma-temperature-gradient, ion-neutral-drag, and Lorentz-force contributions, respectively; for Mars, the black curve shows the inertial term $\partial X_i/\partial t$. Results are shown at 600 km for Earth and 300 km for Mars, close to the respective exobase altitudes.

Solar flares can also temporarily disturb the neutral atmosphere itself (Thiemann et al., 2015). Qian et al. (2019) showed that the 6 September 2017 flares produced measurable changes in Earth's thermosphere during the later stages of the event; such changes in neutral density and temperature feed back into ionization, electron–neutral, and ion–neutral processes, and therefore into the dynamics and energetics of the ionosphere more broadly. Mendillo et al. (2018) reported, for the 10 September 2017 flare, an increase in electron density together with a decrease in electron temperature below 250 km consistent with our results which they attributed to enhanced cooling from an expanded neutral atmosphere combined with inefficient photoelectron heating. Above 250 km, however, their observed electron-temperature increase (exceeding 500 K) was larger than found here, which they suggested might reflect a drop in electron density driven by disturbed solar-wind conditions (Lee et al., 2018), a coupling not represented in our simulations.

The configuration of Mars's crustal magnetic field is a further factor likely to influence ion dynamics that is not captured by our one-dimensional model. Using ASPERA-3 data from Mars Express, Lundin et al. (2011) found that ionospheric O^+ threaded onto strong crustal field lines tends to remain on the dayside, recycling within the resulting crustal "mini-magnetosphere" rather than escaping; consistent with this, the global escape flux is reduced when the strongest crustal-field region faces the Sun (Fan et al., 2019; Dubinin et al., 2020). Both this crustal-field effect and the neutral-atmosphere feedback discussed above warrant further study, but we expect the underlying physical mechanisms identified here to remain valid regardless.

Declaration of Conflict of Interest

The author declares no conflict of interest.

Funding Information

This research received no external funding.

Author Contribution Statement

Ashish Kumar Meena: Conceptualization, Data curation, Formal analysis, Investigation, Methodology, Writing – original draft.

Purushotham Endla: Review

Data Availability Statement

The GOES soft X-ray irradiance data used in this study are available from the NOAA National Centers for Environmental Information (https://www.ngdc.noaa.gov/stp/satellite/goes/) . The Flare Irradiance Spectral Model, Version 2 (FISM2) is available from the Laboratory for Atmospheric and Space Physics (https://lasp.colorado.edu/lisird/data/fism_flare_hr/) . Neutral atmosphere data for Earth were obtained from the NRLMSIS-00 model (https://ccmc.gsfc.nasa.gov/models/NRLMSIS-00/) and neutral wind data from the HWM07 model (https://ccmc.gsfc.nasa.gov/models/HWM-07/) , both distributed by the Community Coordinated Modeling Center. MAVEN NGIMS and LPW observations used for validation of the Martian ionosphere model are available from the NASA Planetary Data System (https://pds-ppi.igpp.ucla.edu/mission/MAVEN). The ionospheric model code and the simulation output underlying the figures in this study are available from the corresponding author upon reasonable request.

References

1. Barton, C. E. (1997). International Geomagnetic Reference Field: The seventh generation. Journal of Geomagnetism and Geoelectricity, 49(2-3), 123-148. https://doi.org/10.5636/jgg.49.123
2. Chamberlin, P. C., Woods, T. N., Eparvier, F. G., & Jones, A. R. (2020). The Flare Irradiance Spectral Model-Version 2 (FISM2) for improved solar irradiance data during flares. Space Weather, 18(12), e2020SW002588. https://doi.org/10.1029/2020SW002588
3. Conway, R. R. (1988). Photoabsorption and photoionization cross sections for solar system aeronomy. Journal of Geophysical Research, 93(A6), 5619-5633. https://doi.org/10.1029/JA093iA06p05619
4. Davies, K. (1990). Ionospheric Radio. Peter Peregrinus Ltd.
5. Drob, D. P., Emmert, J. T., Crowley, G., Picone, J. M., Shepherd, G. G., Skinner, W., Hays, P., Niciejewski, R. J., Larsen, M., She, C. Y., Meriwether, J. W., Hernandez, G., Jarvis, M. J., Sipler, D. P., Tepley, C. A., O'Brien, M. S., Bowman, J. R., Wu, Q., Murayama, Y., Kawamura, S., Reid, I. M., & Vincent, R. A. (2008). An empirical model of the Earth's horizontal wind fields: HWM07. Journal of Geophysical Research, 113(A12), A12304. https://doi.org/10.1029/2008JA013668
6. Dubinin, E., Fraenz, M., Patzold, M., McFadden, J., Halekas, J. S., DiBraccio, G. A., Connerney, J. E. P., Eparvier, F., Chamberlin, P., Duru, F., & Andersson, L. (2020). Induced magnetosphere and its outer boundary at Mars: MAVEN observations. Journal of Geophysical Research: Space Physics, 125(6), e2020JA027958. https://doi.org/10.1029/2020JA027958
7. Fallows, K., Withers, P., & Gonzalez, G. (2015). Response of Mars' ionosphere to solar flares: Analysis of MEX radio occultation data. Journal of Geophysical Research: Space Physics, 120(11), 9805-9825. https://doi.org/10.1002/2015JA021728
8. Fan, K., Fraenz, M., Wei, Y., Han, X., Feng, J., McFadden, J., Rong, Z., Zhong, J., Cui, J., Duru, F., Yu, T., Zhou, B., & Connerney, J. (2019). Effects of the crustal magnetic field on the Martian ionospheric plasma escape. Journal of Geophysical Research: Space Physics, 124(4), 2717-2730. https://doi.org/10.1029/2018JA026346
9. Fennelly, J. A., & Torr, D. G. (1992). Photoionization and photoabsorption cross sections of O, N2, O2, and N for aeronomic calculations. Atomic Data and Nuclear Data Tables, 51(2), 321-363. https://doi.org/10.1016/0092-640X(92)90004-2
10. Fox, J. L., & Bakalian, F. M. (2001). Photochemical escape of atomic carbon from Mars. Journal of Geophysical Research, 106(A12), 30071-30080. https://doi.org/10.1029/2001JA000108
11. Fox, J. L., & Sung, K. Y. (2001). Solar activity variations of the Venus thermosphere/ionosphere. Journal of Geophysical Research, 106(A10), 21305-21335. https://doi.org/10.1029/2001JA000069

12. Fox, J. L., Benna, M., Mahaffy, P. R., & Elrod, M. K. (2021). Comparisons of full diurnal model densities with MAVEN NGIMS data. Journal of Geophysical Research: Planets, 126(2), e2020JE006612. https://doi.org/10.1029/2020JE006612

13. Futaana, Y., Stenberg Wieser, G., Barabash, S., & Luhmann, J. G. (2017). Solar wind interaction and impact on the Venus atmosphere. Space Science Reviews, 212(3-4), 1453-1509. https://doi.org/10.1007/s11214-017-0362-8

14. Gour, P. S., Meena, A. K., Verma, P. L., Soni, S., Sharma, J., & Yadav, V. (2024). Correlation analysis of key parameters associated with solar activity and geomagnetic disturbances throughout 2023. European Academic Research, 11(12), 1494-1504.

15. Huba, J. D., Joyce, G., & Krall, J. (2005). Three-dimensional equatorial spread F modeling. Geophysical Research Letters, 32(20), L20102. https://doi.org/10.1029/2005GL023553

16. Kar, J., Airon, T., & Sudan, G. (1986). Effect of solar flares on the Venus and Martian ionospheres. Advances in Space Research, 6(2), 33-36.

17. Lee, C. O., Jakosky, B. M., Luhmann, J. G., Brain, D. A., Mays, M. L., Hassler, D. M., Holmstrom, M., Larson, D. E., Mitchell, D. L., Mazelle, C., & Halekas, J. S. (2018). Observations and impacts of the 10 September 2017 solar events at Mars: An overview and synthesis of the initial results. Geophysical Research Letters, 45(17), 8871-8885. https://doi.org/10.1029/2018GL079162

18. Lei, J., Liu, L., Wan, W., & Zhang, S.-R. (2004a). Variations of electron density based on long-term incoherent scatter radar and ionosonde measurements over Millstone Hill. Radio Science, 40(2), RS2008. https://doi.org/10.1029/2004RS003106

19. Lei, J., Roble, R. G., Wang, W., Emery, B. A., & Zhang, S.-R. (2004b). Electron temperature climatology at Millstone Hill and Arecibo. Journal of Geophysical Research, 109(A12), A12311. https://doi.org/10.1029/2004JA010600

20. Lei, J., Thayer, J. P., Wang, W., & Burns, A. G. (2007). Studies of thermosphere-ionosphere coupling with SAMI2 and TIME-GCM. Journal of Atmospheric and Solar-Terrestrial Physics, 69(15), 1899-1911. https://doi.org/10.1016/j.jastp.2007.07.011

21. Lollo, A., Withers, P., Fallows, K., Girazian, Z., Matta, M., & Chamberlin, P. C. (2012). Numerical simulations of the ionosphere of Mars during a solar flare. Journal of Geophysical Research, 117(A5), A05314. https://doi.org/10.1029/2011JA017399

22. Lundin, R., Barabash, S., Fedorov, A., Holmstrom, M., Nilsson, H., Sauvaud, J.-A., & Yamauchi, M. (2011). Solar forcing and planetary ion escape from Mars. Icarus, 215(2), 751-758. https://doi.org/10.1016/j.icarus.2011.06.034

23. Martinis, C. R., Wilson, J. K., & Mendillo, M. J. (2003). Modeling day-to-day ionospheric variability on Mars. Journal of Geophysical Research, 108(A10), 1383. https://doi.org/10.1029/2003JA009865

24. Masuoka, T. (1994). Absolute and partial photoionization cross sections of CO2 in the 25-70-eV region. Physical Review A, 50(4), 3078-3087. https://doi.org/10.1103/PhysRevA.50.3078

25. Matta, M., Withers, P., & Mendillo, M. (2014). The composition of Titan's ionosphere. Icarus, 235, 158-169.

26. Meena, A. K., & Gour, P. S. (2024). Investigating Asia's low latitude ionosphere's pulse during the spectacular September 2017 solar storms. Tuijin Jishu/Journal of Propulsion Technology, 45(1), 3322-3334.

27. Meena, A. K., Gour, P. S., & Soni, S. (2024). The effects of strong and weak solar flares on the total electron content in the ionospheric ionosphere during the 2011 solar peak. African Journal of Biomedical Research, 27(4s), 2422-2433. https://doi.org/10.53555/AJBR.v27i4S.2421

28. Meena, A. K., Sharma, A., & Gour, P. S. (2024a). Ionospheric responses to solar flares: An analysis of ion composition changes during Moderately High Solar Activity in January 2023. World Journal of Advanced Research and Reviews, 21(3), 219-224. https://doi.org/10.30574/wjarr.2024.21.3.0618

29. Meena, A. K., Sharma, A., & Gour, P. S. (2024b). The impact of moderate solar flare activity on ionospheric response from August 5th to 7th, 2023. World Journal of Advanced Research and Reviews, 22(01), 043-054. https://doi.org/10.30574/wjarr.2024.22.1.1016

30. Mendillo, M., & Evans, J. V. (1974). Incoherent scatter observations of the ionospheric response to a large solar flare. Radio Science, 9(2), 197-203. https://doi.org/10.1029/RS009i002p00197

31. Mendillo, M., Withers, P., Hinson, D., Rishbeth, H., & Reinisch, B. (2006). Effects of solar flares on the ionosphere of Mars. Science, 311(5764), 1135-1138. https://doi.org/10.1126/science.1122099

32. Mendillo, M., Narvaez, C., Vogt, M. F., Fallows, K., Vitvitsky, A., & Wilkinson, P. (2011). Simultaneous ionospheric variability on Earth and Mars. Journal of Geophysical Research, 116(A11), A11314. https://doi.org/10.1029/2011JA016849

33. Mendillo, M., Huang, C.-L., Pi, X., Rishbeth, H., & Meier, R. (2018). Flares at Earth and Mars: An ionospheric escape mechanism? Space Weather, 16(9), 1235-1251. https://doi.org/10.1029/2018SW001872

34. Mitra, A. P. (1974). Ionospheric Effects of Solar Flares. D. Reidel Publishing Company.

35. Owolabi, C., Chen, G., Zhu, Q., Wan, W., Ni, B., Sun, W., Yang, T., Ren, Z., & Zhang, S. (2020). Ionospheric current variations induced by the solar flares of 6 and 10 September 2017. Space Weather, 18(9), e2020SW002608. https://doi.org/10.1029/2020SW002608

36. Picone, J. M., Hedin, A. E., Drob, D. P., & Aikin, A. C. (2002). NRLMSISE-00 empirical model of the atmosphere: Statistical comparisons and scientific issues. Journal of Geophysical Research, 107(A12), 1468. https://doi.org/10.1029/2002JA009430

37. Pilinski, M. D., Bougher, S. W., Greer, K. R., Thiemann, E. M. B., Andersson, L., Benna, M., & Fowler, C. M. (2021). The global-scale response of the Martian thermosphere/ionosphere system to solar flares. Journal of Geophysical Research: Space Physics, 126(3), e2020JA028631.

38. Qian, L., Wang, W., Burns, A. G., Chamberlin, P. C., Coster, A., Zhang, S.-R., & Solomon, S. C. (2019). Solar flare and geomagnetic storm effects on the thermosphere and ionosphere during 6-11 September 2017. Journal of Geophysical Research: Space Physics, 124(2), 2298-2311. https://doi.org/10.1029/2018JA026175

39. Ren, D., Lei, J., Wang, W., Burns, A., Luan, X., & Dou, X. (2018). Does the strength of the interplanetary magnetic field affect the thermosphere response to a geomagnetic storm? Journal of Geophysical Research: Space Physics, 123(6), 5231-5245.

40. Rishbeth, H., & Garriott, O. K. (1969). Introduction to Ionospheric Physics. Academic Press.

41. Satori, G., Williams, E., & Lemperger, I. (2005). Variability of global lightning activity on the ENSO time scale. Atmospheric Research, 91(2-4), 500-507.

42. Schunk, R. W., & Nagy, A. F. (1978). Electron temperatures in the F region of the ionosphere: Theory and observations. Reviews of Geophysics, 16(3), 355-399. https://doi.org/10.1029/RG016i003p00355

43. Schunk, R. W., & Nagy, A. F. (1980). Ionospheres of the terrestrial planets. Reviews of Geophysics, 18(4), 813-852. https://doi.org/10.1029/RG018i004p00813

44. Schunk, R. W., & Nagy, A. F. (2009). Ionospheres: Physics, Plasma Physics, and Chemistry (2nd ed.). Cambridge University Press.

45. Sharma, D. K., Rai, J., Israil, M., Chandra, H., & Subrahmanyam, P. (2004). Ionospheric response to a solar flare. Indian Journal of Radio & Space Physics, 33, 391-397.

46. Shinagawa, H., & Cravens, T. E. (1989). A one-dimensional multispecies magnetohydrodynamic model of the dayside ionosphere of Mars. Journal of Geophysical Research, 94(A6), 6506-6516. https://doi.org/10.1029/JA094iA06p06506

47. Shinagawa, H., & Cravens, T. E. (1991). A one-dimensional multispecies magnetohydrodynamic model of the dayside ionosphere of Venus. Journal of Geophysical Research, 96(A2), 1149-1162. https://doi.org/10.1029/90JA02237

48. Shinagawa, H., Cravens, T. E., & Nagy, A. F. (1987). A one-dimensional time-dependent model of the magnetized ionosphere of Venus. Journal of Geophysical Research, 92(A7), 7317-7330. https://doi.org/10.1029/JA092iA07p07317

49. Smithtro, C. G., & Solomon, S. C. (2008). An improved parameterization of thermal electron and ion heating rates for use in ionospheric models. Journal of Geophysical Research, 113(A7), A08211. https://doi.org/10.1029/2008JA013080

50. Smithtro, C. G., Sojka, J. J., & Sharber, J. R. (2006). Simulation of the Halloween 2003 solar flare effects in the ionosphere. Journal of Atmospheric and Solar-Terrestrial Physics, 68(18), 2050-2064.

51. Solomon, S. C. (2017). Global modeling of thermospheric airglow in the far ultraviolet. Journal of Geophysical Research: Space Physics, 122(7), 7834-7848. https://doi.org/10.1002/2017JA024314

52. Thiemann, E. M. B., Chamberlin, P. C., Eparvier, F. G., Templeman, B., Woods, T. N., Bougher, S. W., & Jakosky, B. M. (2015). The MAVEN EUVM model of solar spectral irradiance variability at Mars: Algorithms and results. Journal of Geophysical Research: Space Physics, 122(3), 2748-2767.

53. Thiemann, E. M. B., Andersson, L., Lollo, A., Withers, P., Xu, S., Elrod, M., Pilinski, M. D., Ma, Y., Benna, M., Eparvier, F. G., Nagy, A. F., & Jakosky, B. M. (2018). The Mars topside ionosphere response to the X8.2 solar flare of 10 September 2017. Geophysical Research Letters, 45(16), 8005-8013.

54. Todorova, S., Sturrock, P. A., & Nagovitsyn, Y. (2008). Ionospheric responses to solar and geomagnetic events. Advances in Space Research, 42(5), 831-841.

55. Yamauchi, M., Wieser, G. S., Wik, M., Wu, J.-B., & Futaana, Y. (2018). Comparison of solar flare effects on the dayside ionosphere in Sq and non-Sq regions. Journal of Geophysical Research: Space Physics, 123(1), 900-916.

56. Yan, M., Dang, T., Cao, Y.-T., Cui, J., Zhang, B., Liu, Z., & Lei, J. (2022). A comparative study of ionospheric response to solar flares at Earth, Venus, and Mars. The Astrophysical Journal, 939(1), 23. https://doi.org/10.3847/1538-4357/ac92ff